Received: 29 July 2021 | Revised: 10 September 2021 | Accepted: 17 September 2021

DOI: 10.1111/ffe.13587

ORIGINAL ARTICLE

FFEMS Fatigue & Fracture of Engineering Materials & Structures WILEY

Multiaxial static strength of a 3D printed metallic lattice structure exhibiting brittle behavior

Matteo Gavazzoni | **Marco Pisati** | **Stefano Beretta** | **Stefano Foletti**

Dipartimento di Meccanica, Politecnico di Milano, Milan, Italy

Correspondence
Stefano Foletti, Dipartimento di Meccanica, Politecnico di Milano, via La Masa 1, Milan 20156, Italy.
Email: stefano.foletti@polimi.it

Funding information
Italian Ministry of Education, University and Research

Abstract

This paper focuses on numerical the prediction of multiaxial static strength of lattice structures. We analyze a body-centered cubic cell printed with Selective Laser Melting in AlSi10Mg aluminum alloy. Parent material is experimentally characterized, and the Gurson-Tveergard-Needleman (GTN) damage model is calibrated to predict failure in numerical simulations. The GTN model is used to predict failure of the lattice structures exhibiting brittle localized fracture, and it is validated through static tests. The results of experimental tension/compression monotonic tests on lattice samples are compared with the results of numerical simulations performed on as-built geometry reconstructed by X-ray computed tomography, showing a good correlation. Combining the damage model with computational micromechanics, multiaxial loading conditions are simulated to investigate the effective multiaxial strength of the lattice material. Yielding and failure loci are found by fitting a batch of points obtained by some multiaxial loading simulations. A formulation based on the criterion proposed by Tsai and Wu (1971) for anisotropic materials provides a good description of yielding and failure behavior under multiaxial load. Results are discussed, with a specific focus on the effect of as-built defects on multiaxial strength, by comparing the resistance domains of as-manufactured and as-designed lattices.

KEYWORDS

additive materials, aluminum alloy, damage modeling, mechanical properties, multiaxial failure criterion, selective laser melting

1 | INTRODUCTION

Lattice structures are architected materials that show a regular periodicity at the microscale. By properly tailoring their microstructure, a broad variety of physical, thermal, and mechanical properties at the macroscale can be obtained. Macroscopic properties are generally referred to as homogenous or effective properties: They depend on lattice topology, base material, and relative density.[1,2]

Metallic lattice structures are used in a wide range of application fields. The possibility to obtain biocompatible titanium porous structures with elastic modulus close to the one of human bone makes them suitable for implants.[3–9] The high amount of energy that can be

stored during inelastic large deformations can be exploited for impact absorption applications (e.g., bumpers).[10,11] The opportunity to generate porous complex structures through which a fluid can flow also makes lattice structures suitable for heat-exchangers, taking advantage of the improved convection.[12–14]

Identifying the homogenized mechanical properties and predicting the macroscopic mechanical behavior is of primary importance for the use and diffusion of lattice structures. It is well known that detailed simulation of a component with lattices can be unaffordable when using standard computers and tools.

Prediction of homogenized linear elastic properties is a well-addressed topic in literature. For simple 2D and 3D low-density strut-based lattices, several theoretical models are available in literature.[1,2,15–17] In these formulations, lattice struts are modeled as beams. Comparing theoretical predictions with experimental results, it was observed that these models can be used only if lattice beams are sufficiently slender.[18] For more complex and general lattice structures, elastic properties are computed by means of numerical models based on the application of Asymptotic Homogenization theory.[19–21]

Yielding of metallic lattices has been thoroughly studied, as well. Theoretical models were built to predict uniaxial and multiaxial plastic collapse of honeycombs and three-dimensional lattices.[1,15,22] Other works used computational micromechanics to provide the yielding locus of lattice structures. An example is the work of Lee et al.,[23] in which yielding under multiaxial loading conditions of an as-designed Schwarz-primitive surface-based lattice structure is studied numerically and yielding locus is fitted using an extension of the Hill's anisotropic yielding function.

A limited number of works can be found in literature about predicting static ultimate strength of lattices. In their seminal work, Gibson and Ashby[1] provided theoretical prediction of the strength of hexagonal honeycombs made of brittle materials. More recently, the uniaxial strength of lattice structures and foams has been studied numerically, by modeling the lattice as a set of beams and applying proper criteria to account for failure[24] or by implementing damage models to account for local fracture in 3D solid elements models.[25–27] However, multiaxial strength of lattices exhibiting brittle behavior is a not fully addressed topic yet very important when designing with this kind of structures.

Additive manufacturing processes (3D printing) allow to fabricate complex structure with small features that cannot be obtained by traditional processes. However, as-built geometry obtained with these processes may differ from as-designed geometry, as a consequence of process induced defects. Defects strongly affect the mechanical response of 3D printed lattice structures: They can be material defects (micro-voids, lack of fusion, surface roughness, etc.) or geometric defects (irregular geometry, missing struts in lattice cells, etc.).[28,29] Some works studied numerically the sensitivity of mechanical properties, such as elastic modulus and plastic collapse, to as-designed defects, i.e., geometry perturbations introduced to get knock-down factors instrumental for the design phase.[30–32] On the other hand, other works studied the effect of as-manufactured defects, by characterizing the geometry obtained by the printing process.[25,33–35] In the comprehensive work of Liu et al.,[34] defects are statistically characterized, and their effect on mechanical response and failure mechanism in compression is found for different strut-based 3D lattices. However, the difference between multiaxial strength of as-designed and as-manufactured geometry is still an open point. Given the difficulties that could arise in experimental testing lattices under multiaxial loads and the impossibility to obtain a defect-free geometry, quantifying this effect numerically is fundamental.

In this work, we address the multiaxial strength of imperfect lattices with brittle behavior. We propose a numerical method to characterize lattice strength and to obtain yielding and failure loci. We examine a body centered cubic cell, named SC-BCC according to the nomenclature given in Tancogne-Dejean and Mohr,[36] obtained by Selective Laser Melting (SLM) with AlSi10Mg aluminum alloy. The failure in compression for this cell made of aluminum is driven by local fracture, and neither buckling nor plastic collapse was observed.[37] The base material is characterized, and the Gurson-Tveergard-Needleman (GTN) damage model for porous metal is calibrated to predict failure in numerical simulations. The damage model is validated by comparing experimental tensile and compression tests on lattice samples with numerical simulations performed on as-built geometry reconstructed from X-ray computed tomography. By combining computational micromechanics with the GTN model, the multiaxial strength is studied. Numerical failure locus and yielding surface are identified for multiaxial loading conditions. We found that the tensor polynomial criterion for composites proposed by Tsai and Wu[38] gives an accurate fitting of the numerical points. Results are discussed focusing on the effect of as-built geometry on multiaxial strength.

2 | EXPERIMENTAL INVESTIGATION

Tensile tests were carried out on parent material to characterize it and to set a reference for the calibration of the

damage model used in numerical analyses. Tension and compression tests were performed on lattice samples to validate the damage model calibrated for parent material.

All the specimens were printed in AlSi10Mg powder, with a SLM Solutions 280 v1.0 printer. The power of the laser was set to 350 W, scanning speed of 1,150 mm/s, with a layer thickness of 50 μm, and hatching distance of 0.17 mm. The process parameters were selected as the result of an optimization procedure for printing lattice structures. Consistency of process parameters was ensured for all the samples.

2.1 | Parent material characterization

Parent material characterization was performed on small-scale dog-bone tensile samples. Samples have nominal section dimension of 1.2×3 mm and gauge section of 7 mm. We chose this specimen geometry to get as close as possible to the dimension of the lattice struts (0.6 mm) without increasing excessively the complexity of the test. In fact, it is well known that in metal additive manufacturing processes, the dimension of the features may impact the microstructure and consequently the mechanical properties.[39] Two different groups of specimens were tested: The first was printed vertically, while the second was inclined at 45° to the growth direction. Some of the specimens were polished, while others were tested as-built. Tests were performed with a 1kN electromechanical testing machine at a strain rate of 0.0007 s^{-1}. Digital Image Correlation (DIC) was performed in the central part of the gauge section to measure the strain by means of a virtual extensometer and to study strain localization at failure to be compared with numerical analysis (see Section 3.1 and Figure 1). A high-resolution camera with a specific set of lenses was used, with a field of view of 13.5×10 mm and a resolution of 8.3 μm/pixel. The software Vic-2D form Correlated Solutions has been used to analyze the results.

Before testing, the specimens were analyzed by CT scanning, at a resolution of 7 μm/voxel. The CT scan used is a 300 kV, double X-ray tubes, Baker Hughes GE Phoenix VtomexM. A reconstruction of the scan for an as-built specimen printed vertically together with a cross-sectional view is shown in Figure 2A. The contour of the section is not rectangular and appears quite irregular. Moreover, two types of defects were found in all the specimens: pores (detail A) and lack of fusion (detail B). To quantify the presence of defects in the volume, a porosity analysis was performed, and the results are reported in Figure 2B. Porosity was measured by applying a sharp filter to the gray-scale slice images of CT scan (Figure 2A) to clearly distinguish voids from material and to quantify their presence. The average void volume fraction (VVF), defined as the volume of voids over the overall volume, is around 0.45%, and no significant difference in terms of amount, dimension, and shape of the defects was observed between the specimens printed vertically and those inclined at 45°.

Figure 3A,B shows the tensile curves of the material, Figure 3C shows the scanning electron microscope (SEM) analysis of the fracture surface of Sample 2, and Table 1 reports the material properties, with mean value, standard deviation, and coefficient of variation.

For the computation of material properties, curves obtained with specimens printed at 45° with as-built surfaces (Samples 7 and 8) were discarded. For these two samples, failure happened in the transition from the gauge section to grips, as small notches were left by the removal process of supports needed to print the

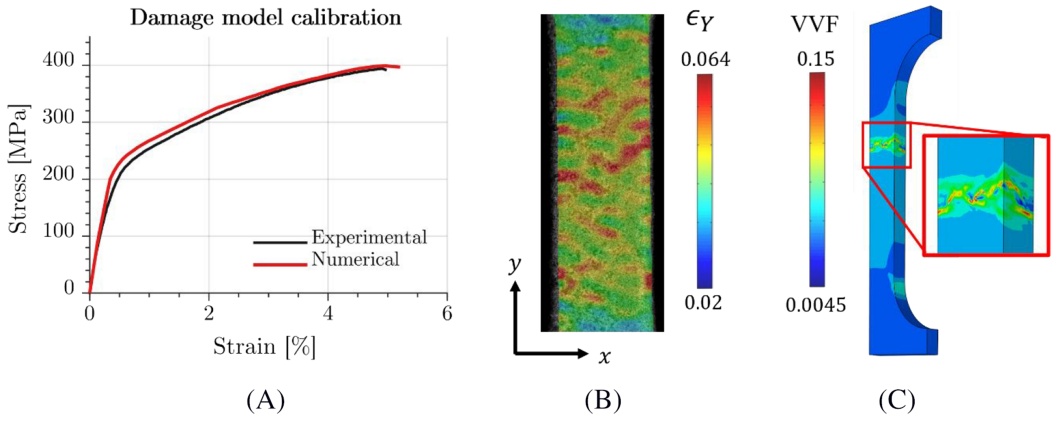

FIGURE 1 GTN model calibration on parent material tensile tests: (A) experimental tensile curve compared with numerical results, (B) strain localization captured by DIC during the experiments, and (C) numerical fracture surface predicted by the damage model [Colour figure can be viewed at wileyonlinelibrary.com]

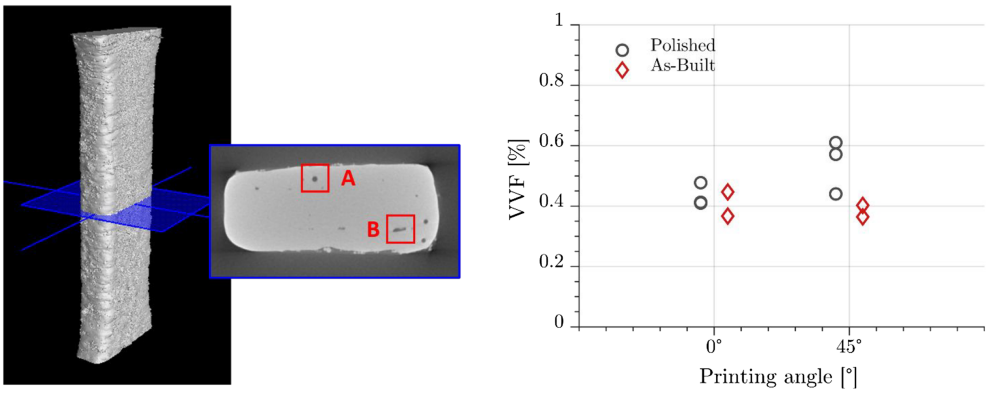

FIGURE 2 CT scan analyses of parent material tensile specimens: (A) reconstruction and cross-sectional view, highlighting a pore (detail A) and a lack of fusion (detail B); (B) results of porosity analysis (voids volume fraction in percentage vs. printing angle) [Colour figure can be viewed at wileyonlinelibrary.com]

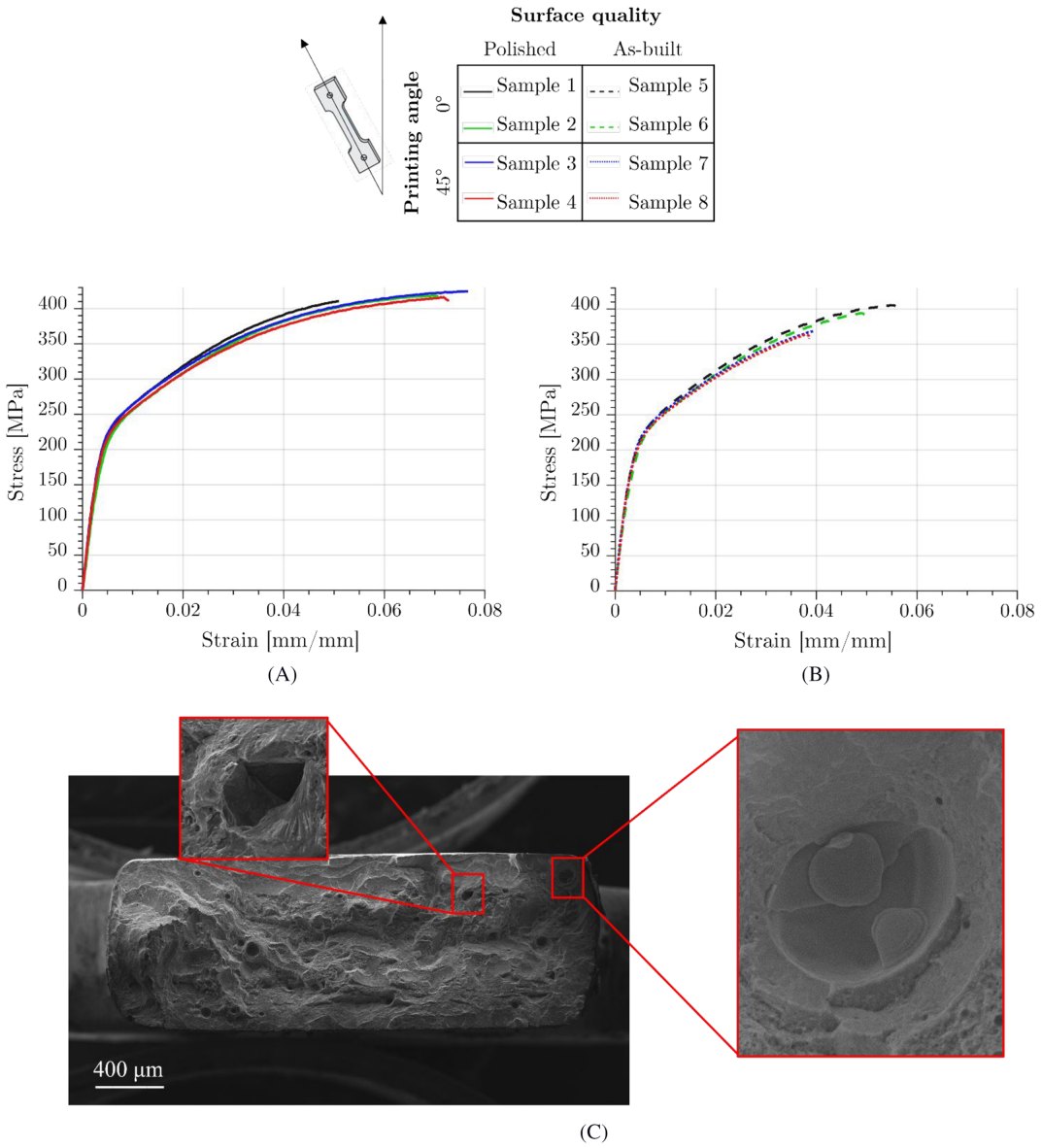

FIGURE 3 AlSi10Mg tensile curve obtained from dogbone specimens printed at different printing angles and with different surface qualities (A, polished surface; bB, as-built surface); (C) SEM images of fracture surface of Sample 2, highlighting the presence of internal defects on the fracture surface [Colour figure can be viewed at wileyonlinelibrary.com]

specimens with an angle of 45°. This effect is not present for Specimens 3 and 4, as surface polishing removed the notch left by supports.

For Samples 1 to 6, the experimental scatter is limited, and all the curves are close. No significant dependence of the stress-strain curves on the printing angle and surface quality can be observed on these small-scales samples. The coefficient of variation is small for elastic modulus, yielding stress, and ultimate tensile strength (UTS), while it is higher for the strain at failure. The higher variation of the latter quantity can be attributed to the presence of micro-voids and lack of fusion that might play a role in fracture initiation, as can be observed looking at the fracture surface of Sample 2 in Figure 3B. However, a detailed analysis of the fracture mechanism of parent material to quantify these effects is out of the scope of this work.

2.2 | Monotonic compression and tensile tests on lattice samples

The lattice structure we examine in this work is a body-centered cubic cell, named as SC-BCC.[36] Figure 4A shows the periodic unit cell. The length of the cell is 2.4 mm with a strut diameter of 0.6 mm, giving an as-designed relative density of 35.6%. This topology was studied in some literature works (e.g., Tancogne-Dejean & Mohr[36]) and was already selected, with this combination of geometric parameters,[37,40,41] as a case study in our previous works. Figure 4B shows the geometry of the specimens used for the experiments. Specimens are provided with grips allowing to apply both tension and compression load and to avoid non-linearities in the first part of the compression stress-strain curve due to contact between compression plates and specimen ends.[37]

To limit the overhang angle of all the struts of the lattice structure, specimens were printed with an inclination of 45° with respect to the vertical specimen axis (i.e., the direction of the load) and 22.5° with respect to one of two other axis. The specimens have a cross-sectional area of 4 × 4 cells (around 10 × 10 mm) with four cells in height that have constant density and two layers of cells per side with graded density, in order to smooth the transition between the lattice and the grips and to localize failure in the central region.[42,43] Graded density is obtained by linearly increasing the struts diameter, from 0.6 to 0.8 mm in the first layer and from 0.8 to 1.2 mm in the second one. The number of cells in section and in height was chosen to match the constraints imposed by manufacturability, manufacturing costs, and testing facilities (testing machine and DIC equipment) limits and to allow numerical simulations of the entire specimen to validate the damage model. We emphasize that the primary target of these experiments is to validate the damage model implemented in the numerical models. Obtaining an experimental curve that renders the homogenized behavior of the material is not the main focus: The difference with homogenized behavior will be evaluated by comparing the results with numerical simulation of a single unit cell with periodic boundary conditions (PBC).

TABLE 1 Parent material properties obtained from Specimens 1 to 6: Mean value μ, standard deviation σ, and coefficient of variation CV = μ/σ for elastic modulus, yielding stress, ultimate tensile strength (UTS), and strain at failure

	μ	σ	CV
Elastic modulus (MPa)	68,000	1,000	1.5%
Yielding stress (MPa)	220	7.3	3.3%
UTS (MPa)	410	11.4	2.8%
Strain at failure (%)	6.2	1.1	16.7%

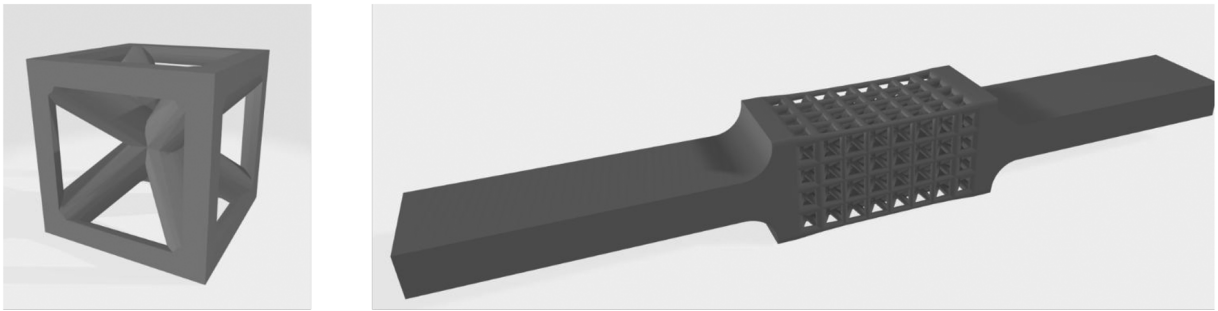

(A) (B)

FIGURE 4 (A) SC-BCC unit cell and (B) specimen geometry with graded density to smooth transition between lattice and grips, used for monotonic tension and compression tests

Before the mechanical testing, one of the specimens (Specimen 1 tested in compression) was analyzed with CT scan to evaluate the deviation of as-manufactured geometry from the as-designed and to reconstruct the as-manufactured geometry for numerical analyses (see Section 3). Figure 5A shows the 3D reconstruction of the scan, together with its vertical section, Figure 5B, from which it is possible to observe higher presence of pores if compared to the tensile specimen in Figure 2, as well as irregular struts borders and randomly distributed imperfections. We performed a micro-porosity analysis, as done for the dogbone samples, obtaining a void volume fraction of 2%. Moreover, we found that as-manufactured structure is oversized with respect to as-design geometry, with a relative density of 38.9%. Relative density of as-manufactured cell was computed by weighting with a high precision scale a sample specifically designed for this purpose, without grips and with cells at constant relative densities, printed in the same job of the specimens used for mechanical testing. As-manufactured geometry is about 3% more dense than the as-designed one (9% of relative increase), hence showing an oversizing of the geometry induced by the manufacturing process.

Monotonic tests were conducted in displacement control with a 10 kN MTS electromechanical testing machine at a constant strain rate of approximately 0.00025 s^{-1}. Three-dimensional Digital Image Correlation (DIC) was performed on one face of the specimen to measure the homogenized strain and to better understand the failure mechanism. The Aramis system by GOM was used, with a three-dimensional field of view of 110 × 100 × 20 mm.

Figure 6A,B shows the results of compression tests. Three tests were carried out. The homogenized strain for the stress-strain curve (Figure 6A) was obtained placing a virtual extensometer in the central part of the specimen with a length of four cells. During the test, no buckling phenomena were observed, and failure is driven by a localized fracture inside the lattice (Figure 6B). Locally, failure happens on the horizontal struts (red circle), subjected to tensile load because of lateral expansion of the cell. Globally, the specimens fail at a plane inclined at 45° (dashed red line), resulting in a planar fracture surface. The same failure mechanism was observed for the all the tested specimens. These experimental results are in agreement with what was observed in previous works on the same lattice structure.[37]

Monotonic tensile tests on lattice samples were carried out using the test method and the specimen-geometry described for compression tests. Also in this case, three samples were tested. Figure 6C shows the stress-strain curves of the three tests, while Figure 6D shows the broken specimen configuration. In this case, the structure fails locally because of vertical struts failure, as they are subjected to tensile load. Globally, the failure happens almost on the same cell row on the frontal face. However, no clear disposure of the broken struts can be recognized, as in the case of compression load. The strain at failure is considerably lower in tension than in compression.

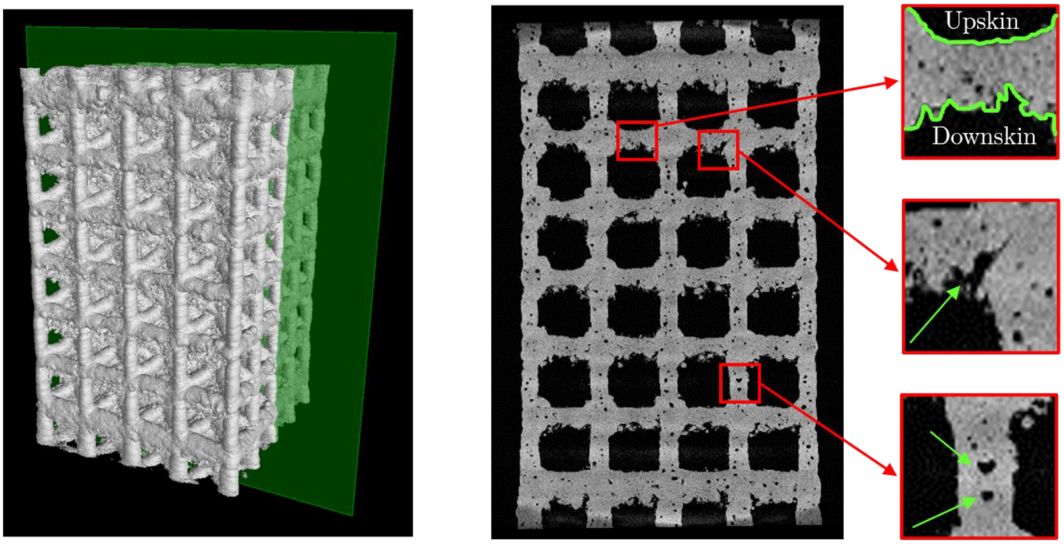

FIGURE 5 Lattice specimen CT scan analysis: (A) volume reconstruction; (B) vertical section slice view showing irregular strut borders, randomly distributed imperfections, and micro-porosity [Colour figure can be viewed at wileyonlinelibrary.com]

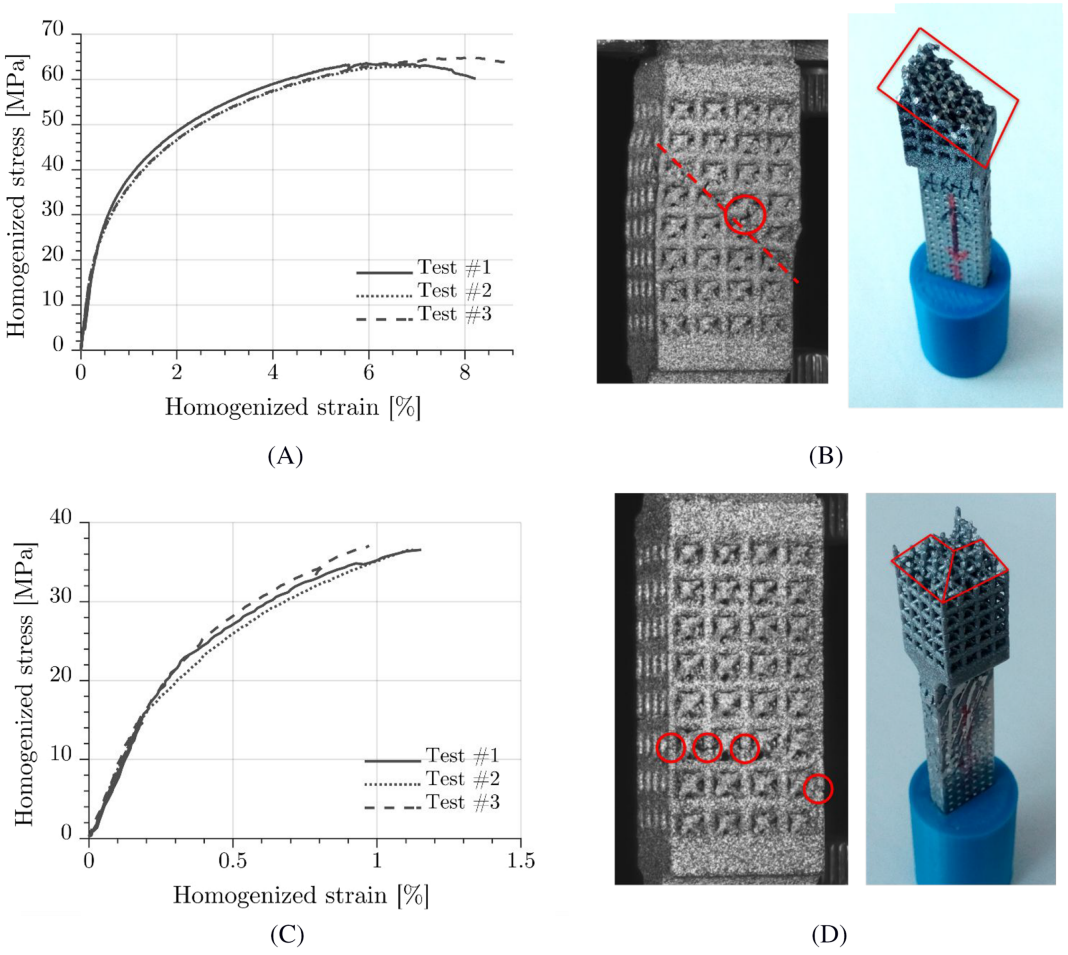

FIGURE 6 Homogenized stress-strain curves for (A) compression and (C) tensile tests performed on lattice samples. Broken specimen configuration and fracture surface for (B) compression (Test 1) and (d) tension (Test 1) [Colour figure can be viewed at wileyonlinelibrary.com]

TABLE 2 Mechanical properties of SC-BCC lattice structure computed from tension and compression experimental curves: Mean value and standard deviation in brackets

	Tension	Compression
Elastic modulus (MPa)	8,750 (218)	8,730 (151)
Yielding stress (MPa)	27.57 (1.37)	28.29 (1.80)
Ultimate strength (MPa)	36.78 (0.28)	63.86 (0.96)
Strain at failure (%)	1.11 (0.12)	6.95 (1.07)

Table 2 shows a comparison of the homogenized mechanical strength both for tension and compression. The elastic modulus was computed by linearly interpolating the linear part of the curve, while the yielding stress was computed as the stress that corresponds to a plastic strain of 0.2%. The results in tension and compression are almost identical for the elastic modulus and the yielding stress. However, the different failure mechanism and damage evolution inside the structure lead to a strong difference between the ultimate strength and the strain at failure in tension and compression.

3 | NUMERICAL ANALYSES

The aim of the numerical analyses of this work is two-fold: first, to study the multiaxial ultimate strength of our lattice structure and to identify a yielding and failure locus and, second, to quantify the differences on the multiaxial mechanical response between as-designed lattice geometry and as-manufactured geometry obtained by the printing process.

In this section, we calibrate the Gurson-Tveergard-Needleman (GTN) to reproduce the parent material behavior up to failure, as experimental test on lattice samples showed that failure of our structure is ruled by localized fracture (Section 2.2). The model is validated comparing tension/compression experimental results with increasing-complexity numerical simulations

(Section 3.2). Finally, we build single cell models with periodic boundary conditions under multiaxial states of stress, to identify some numerical points to fit the yielding surface and failure locus (Section 3.3). For all the analyses, the commercial finite element software Abaqus[44] is used.

3.1 | Damage model calibration

To predict failure in numerical simulations, we adopted the GTN damage model for porous metals.[45–49] The GTN model is already implemented in several commercial FE codes (e.g., Abaqus and Ansys) and predicts failure because of growth, nucleation, and coalescence of micro-voids inside the material. The parameter that rules failure is the void volume fraction (VVF) that quantifies the presence of micro-voids in each element of the model. The VVF evolves during the loading phase according to the constitutive equations. If the VVF reaches the critical value in one element, that element loses its load-bearing capacity. Recent works showed that failure of aluminum lattice structures and foams under uniaxial compression can be well predicted using this model.[25,26]

To calibrate the damage model parameters, we simulated the tensile tests performed on parent material dogone samples in Abaqus\Explicit. The stress-strain curve obtained for Sample 5 (as-built surface and printed vertically) was used as a reference for the calibration process. One quarter of as-designed specimen's geometry was modeled, exploiting two planes of symmetry. C3D10 explicit elements were used with an approximate mesh size of 0.07 mm. The elastic modulus of the material was set to 68,000 MPa, according to the experimental results, with a Poisson ratio of 0.3, while the plastic law was extrapolated from the tensile test curve, and it was entered in Abaqus as a tabular isotropic hardening law. Nucleation and failure options for the GTN model were activated. The initial void volume fraction (parameter f_0) was set at 0.45%, according to the values given by the porosity analyses of CT scans (Figure 2B). The three material parameters q_1, q_2, and q_3 were set at 1.5, 1, and 2.25, respectively, as indicated in Tvergaard.[50] Failure ($f_F = 0.125, f_c = 0.007$) and nucleation parameters ($\epsilon_n = 0.057, s_n = 0.01, f_N = 0.04$) were identified by means of a trial-and-error method, comparing the stress-strain curve obtained from the numerical analysis with the experimental reference curve.

Figure 1 shows the results of the damage model calibration, in terms of characteristic curves (Figure 1A), comparison between two-dimensional DIC strain localization (Figure 1B) and fracture surface, identified by the highest values of the variable VVF (Figure 1C).

3.2 | Damage model validation

To test and validate the accuracy of damage model in predicting local failure under state of stress different from the simple uniaxial tension, we replicated numerically the compression and tension experiments on lattice samples. Even if the lattices are subjected to homogeneous uniaxial tension (or compression), cell topology leads to local stress multiaxiality.

To simulate the homogenized response in tension/compression of the lattice structure, single-cell models were developed, both on as-designed and as-manufactured geometry. As-manufactured geometry was obtained from the CT scan of Specimen 1 tested in compression (Figure 5) by applying a sharp filter so as to obtain a value of relative density that parallels the experimental one (38.9%) and by reconstructing the geometry with a mesh suitable for finite element analyses. Internal defects were not modeled because their effect is considered in the parameter f_0 of the GTN model that represents the initial void volume fraction of the material. Thus, for lattice numerical simulations, f_0 was set to 0.02, according to the result of the porosity analysis performed on CT scan of lattice sample. Periodic boundary conditions (PBC) were applied to render the mechanical behavior of a homogeneous mean not affected by boundaries. PBC were implemented coupling the degrees of freedom of different points on opposite faces of the reference volume element with a proper set of equations.[51–53]

Three models with different complexity and boundary conditions were built with as-manufactured geometry to simulate the mechanical response of the specimen in tension and compression (Figure 7). One eighth of the central part of the specimen was simulated, exploiting the presence of three planes of symmetry, as shown in Figure 7A. However, exploiting symmetries does not make it possible to catch the inclined fracture plane experimentally observed in compression. Thus, to better understand if the failure mechanism of the structure is correctly described by the damage model, one vertical row of cells of the specimen was simulated. The model is shown in Figure 7B. Periodic boundary conditions were applied in the Y direction; i.e. this model is representative of a structure having four cells in the X and Z directions and an infinite number of cells in Y. Finally, the entire specimen was modeled (Figure 7C): Four cells in the height of constant relative density and one row of cell with graded density per side were considered.

For all the numerical analyses, C3D10 explicit elements were used with an approximate mesh size of 0.07 mm, to ensure consistency with the calibration model of parent material tensile test described above. A preliminary convergence analysis conducted on single

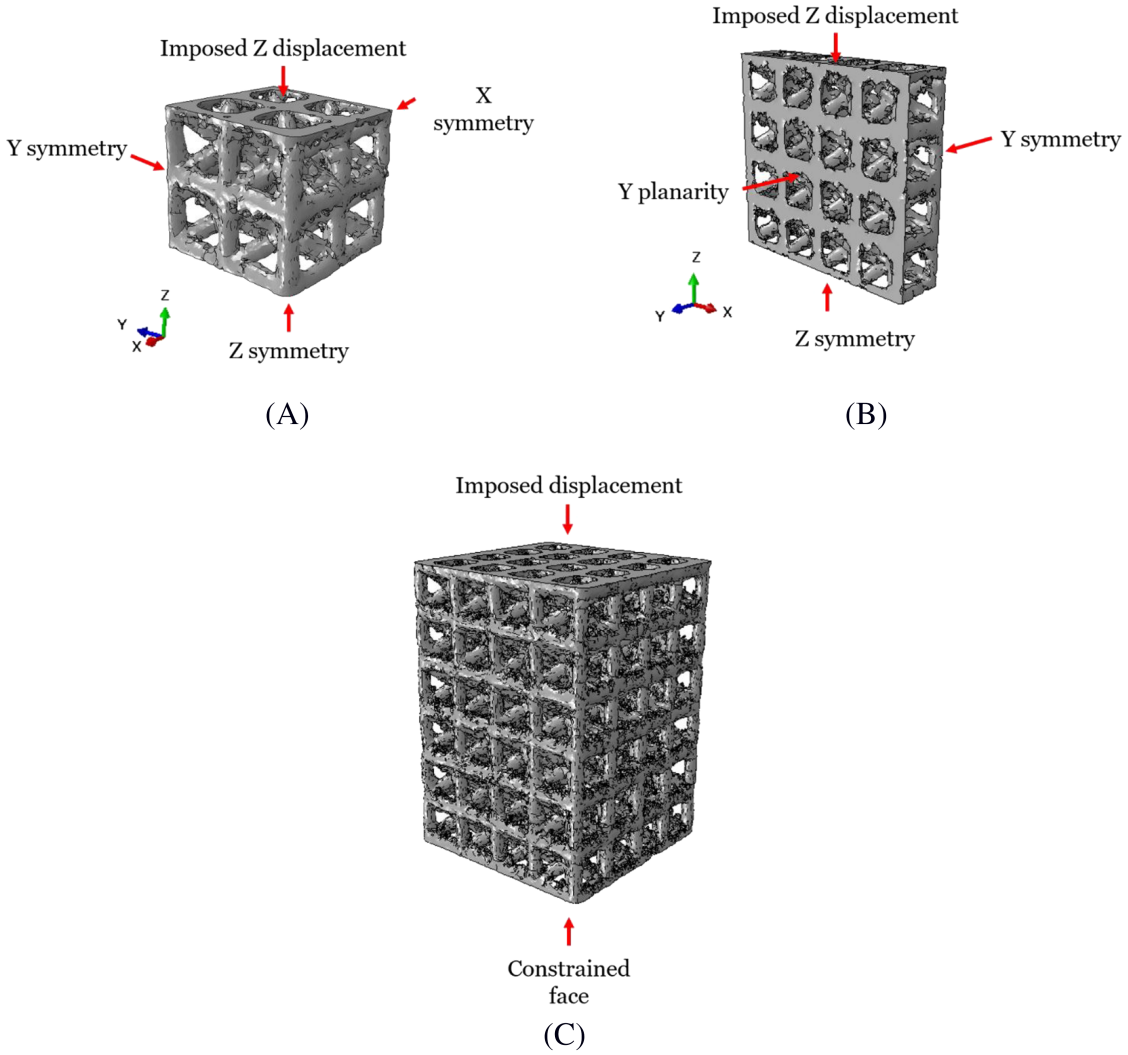

FIGURE 7 Numerical models for as-manufactured geometry lattice sample: (A) 1/8 of specimen with symmetries, (B) one row of specimen with periodic conditions in *Y*, and (C) entire specimen with one layer per side of cells with graded density [Colour figure can be viewed at wileyonlinelibrary.com]

cell model showed that the results are stable for mesh sizes lower than 0.09 mm.

Figure 8 shows the results of the increasing-complexity analyses in compression. Looking at the stress-strain curves plot (Figure 8A), we observe a significant difference between the response of as-designed single cell with PBC (dotted green line) and as-manufactured single cell with PBC (dashed green line). At equal strain, the stress predicted by the as-designed cell is about 15% lower than the one for the as-manufactured cell model, because of the different relative densities. The strain at failure is approximately 30% lower for the as-manufactured cell, as a consequence of irregular struts borders and random imperfections that lead to strain localizations and act as fracture triggers. Single cell with as-manufactured geometry curve lies below the experimental response (approximately 5–10%), showing the slight difference between the homogenous response and the structural response of the samples. When modeling the specimen with the three models in Figure 7, the prediction of the characteristic curve practically overlaps the experimental curve (blue and red curves).

The single-cell model and the eighth of specimen model are able to describe the local failure mechanism, i.e., the tensile failure in the horizontal struts (red circles in Figure 8B). However, as expected, the presence of periodic and symmetry boundary conditions does not make it possible to describe the global failure mechanism. By modeling one vertical row (Figure 8C), it is possible to observe that the horizontal broken struts are laid out on a line inclined at 45°. The inclined failure plane is clearly visible from the results of the entire specimen model simulation, in Figure 8D, in agreement with the experimental observation reported in Figure 6B.

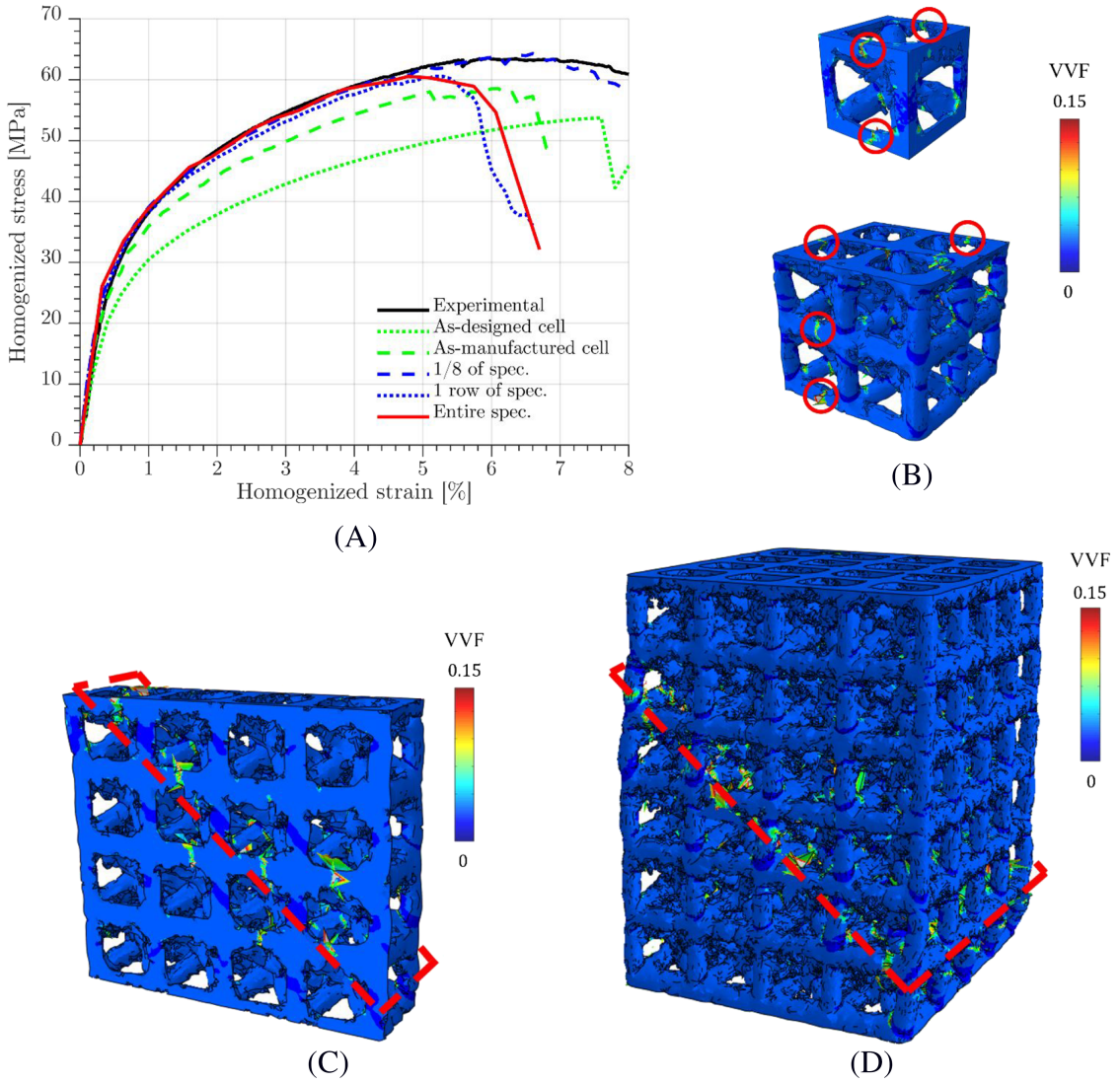

FIGURE 8 Results for increasing complexity numerical models in compression: (A) homogenized stress-strain curves compared with experiments, failure localization (VVF color plot) for (B) single cell, and 1/8 of specimen model, (C) single vertical row of cells, and (D) entire specimen. In the numerical models, the load was applied in the vertical direction [Colour figure can be viewed at wileyonlinelibrary.com]

The results for tensile load condition are shown in Figure 9. The difference in the stress-strain curves (Figure 9A) between single cell models with as-designed and as-manufactured geometry is significant and more severe than what observed for compression. In particular, the strain at failure of the as-designed cell is 2.5 times higher than the one of the as-manufactured cell, indicating more severe effects of irregular struts borders and random imperfections for this loading condition. The prediction given by the sample models (dashed and dotted blue lines) is close to the experimental curve, and no significant difference can be observed between them. In the single-cell model (Figure 9B), failure occurs on the vertical struts subjected to tensile load in correspondence with geometrical imperfections. Referring to the vertical row model, in Figure 9C, failures on the vertical strut of the different cells, highlighted with red circles, are randomly distributed in the structure, as for the experiments.

3.3 | Multiaxial load numerical models

The results reported above show that the GTN damage model can be used to predict the response of the lattice structures up to failure. Single-cell models with as-manufactured geometry correctly describe the cell local failure mechanism and provide predictions of the experimental curves with sufficient accuracy (less than

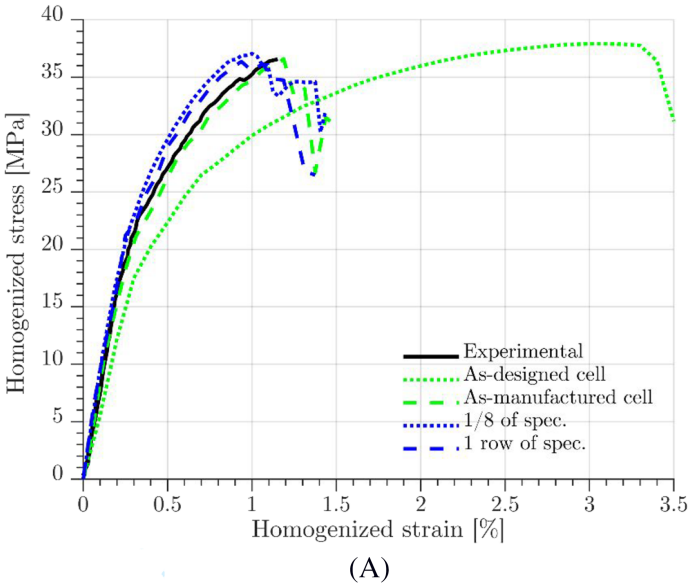

FIGURE 9 Results for numerical simulations of tensile loading conditions: (A) stress–strain curves, failure localization (VVF color plot) for (B) single cell model with as-manufactured geometry, and (C) for single row of cells model (load is applied in vertical direction) [Colour figure can be viewed at wileyonlinelibrary.com]

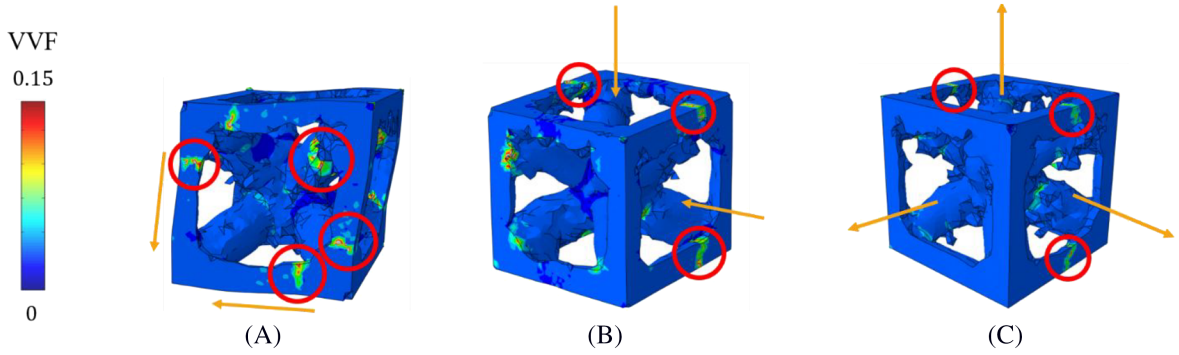

FIGURE 10 Multiaxial loading condition simulations: localization of failure for (A) shear condition, (B) biaxial compression, and (C) positive triaxial condition [Colour figure can be viewed at wileyonlinelibrary.com]

10% error). Hence, we extended the single-cell models with PBC and as-manufactured geometry to multiaxial loading condition to study numerically the multiaxial ultimate strength of our lattice structure. The simulations reported in this section are instrumental to the definition of a closed form yielding and failure locus. We emphasize that, as no relevant works in literature addressed the experimental characterization of lattice structures under multiaxial loading conditions, numerical analyses play a crucial role in the definition of a criterion to assess static multiaxial strength and yielding.

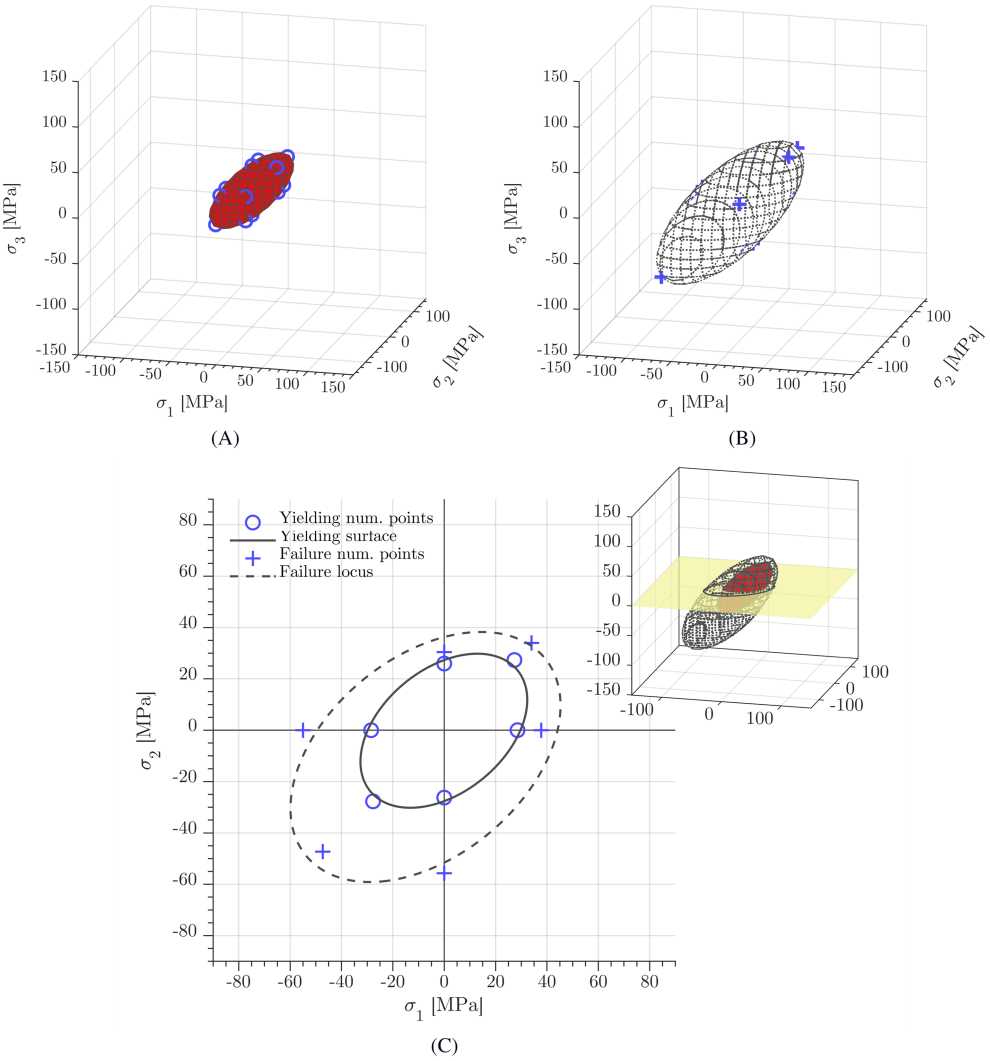

FIGURE 11 As-manufactured cell geometry (A) yielding and (B) failure locus in $\sigma1$—$\sigma2$—$\sigma3$ space and (C) for plane stress conditions ($\sigma3 = 0$). The analytical description of the locus is compared with the numerical points used for the fitting [Colour figure can be viewed at wileyonlinelibrary.com]

The results of three simulations for three different multiaxial loading conditions are shown in Figure 10, in which the VVF variable is plotted. Figure 10A shows the results for shear condition in *X*-*Y* direction. Failure is localized at the diagonal strut close to the central nodes that is subjected to tensile loading and on the vertical struts that are subjected to bending. The yielding limit in shear is 21.8 MPa (81% of the uniaxial stress yielding limit in *Z* direction), while the ultimate shear strength is 30.6 MPa (83% of the tensile ultimate strength, *Z* direction). Figure 10B shows the results for the case in which an equal negative stress was applied in directions *X* and *Y* ($\sigma_1 = \sigma_2$). Failure happens in the struts oriented in the third direction because of lateral expansion due to the loads, similarly to the case of simple compression (see Figure 8B). In Figure 10C, the results for the positive hydrostatic stress case are shown. In this case, failure happens in the most loaded struts, in correspondence of geometrical imperfections.

4 | NUMERICAL YIELDING AND FAILURE LOCUS

To identify a sufficiently large number of numerical points onto which a failure locus can be fitted, we simulated several multiaxial loading conditions. Numerical analyses for simple compression and tension loads applied in different directions revealed that the homogenized behavior of as-manufactured structure is slightly anisotropic, as manufacturing defects lead to a geometry that is not cubic symmetric as the as-designed one. It was found that a formulation based on the tensor polynomial criterion proposed by Tsai and Wu[38] well describes this lattice structure yielding and ultimate strength:

$$F_i\sigma_i + F_{ij}\sigma_i\sigma_j = 1, \tag{1}$$

where i,j = 1,...,6, σ_i are the stress components in the principal orthotropic directions ($i = 1,2,3$ normal stress

components, $i = 4,5,6$ shear stress components) and F_i, F_{ij} are the material strength coefficients. Assuming a failure insensitive to the sign of the shear stresses, all terms containing a linear term of shear stress vanish, leading to the following explicit form of the general expression:

$$F_1\sigma_1 + F_2\sigma_2 + F_3\sigma_3 + F_{11}\sigma_1^2 + F_{22}\sigma_2^2 + F_{33}\sigma_3^2 + F_{44}\sigma_4^2 + F_{55}\sigma_5^2 + F_{66}\sigma_6^2 + 2F_{12}\sigma_1\sigma_2 + 2F_{13}\sigma_1\sigma_3 + 2F_{23}\sigma_2\sigma_3 = 1. \quad (2)$$

The coefficients F_{ij} and F_k were fitted using the least squared error method. It was found that all shear cases, uniaxial, biaxial, triaxial tension, and compression cases represent the smallest set of simulations (17 overall) which allows a sufficiently accurate identification of the failure surface. Using this set of simulations, it is possible to describe the interplay role of the simultaneous presence of normal stresses applied in different directions and to catch the different failure mechanism for shear conditions. Being the material anisotropic due to manufacturing defects, all the possible combinations of loading directions must be simulated.

The yielding surface was fitted with the same procedure. The yielding condition from numerical simulations was defined by means of an energetic approach used in literature for solid materials (e.g., Banabic et al.[54]). The plastic energy density is defined as

$$W_p = \sum_{i=1}^{6} \int \sigma_i \, d\epsilon_i^{pl},$$

where ϵ_i^{pl} is ith component of the plastic strain vector. The value at 0.2% of plastic strain for uniaxial tension along X direction has been set as a reference. For the other cases, yielding point has been defined taking the stress at the instant at which the plastic energy density equals the reference.

The yield surface found according to Equation 2 is plotted in Figure 11A in the $\sigma_1 - \sigma_2 - \sigma_3$ space, together with the numerical points used for the fitting. The surface is an ellipsoid with the three axes rotated in relation to the principal ones. The ellipsoid is centered in the origin; thus, the material is symmetrical for yielding, according to tension/compression experiments and numerical simulations. A consequence of this aspect is that the linear terms F_1, F_2, and F_3 for the yielding surface equation have a very low value if compared to the quadratic terms. In Figure 11B, the failure locus is shown. The surface is an ellipsoid too but not centered in the origin, as the material is nonsymmetric at failure.

The section views of the two surfaces for $\sigma_3 = 0$ are shown in Figure 11C. The shape of yielding surface in this plane is similar to the Von Mises ellipse. The main difference is that, for this lattice structure, yielding occurs for the hydrostatic loading condition as well. Failure and yielding surfaces are closer if one of the two applied stress is positive (I, II, and IV quarters) while the distance between the two increase if both the applied stresses are negative, showing a strong detrimental effect of a positive stress on the ultimate strength.

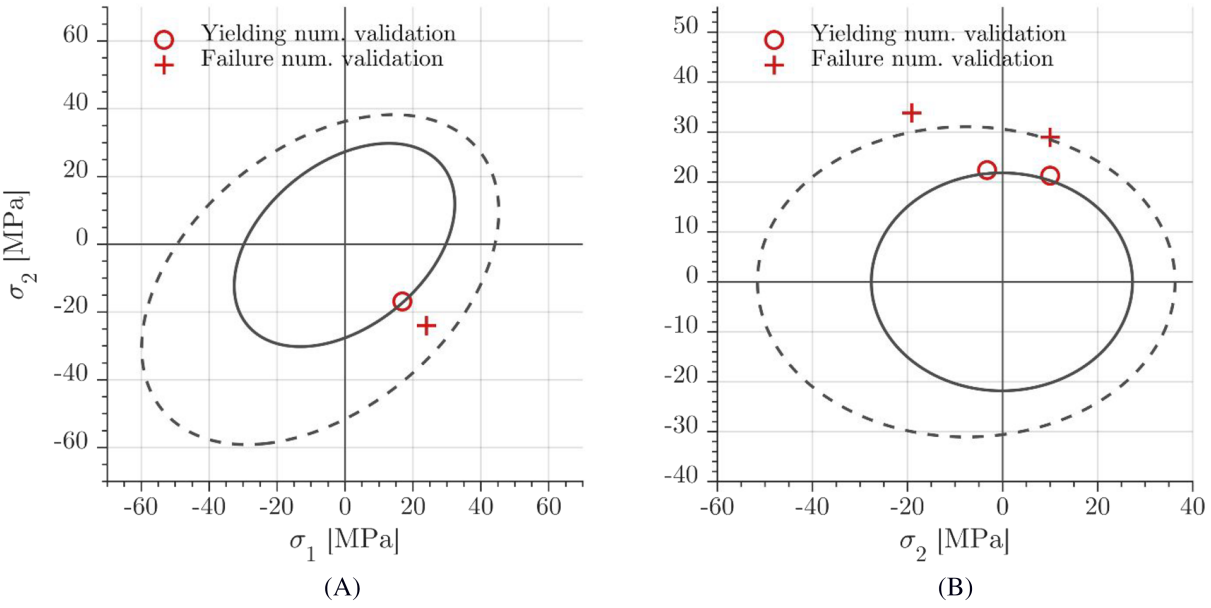

FIGURE 12 Yielding and failure locus validation, graphical representation in planes (A) $\sigma1$—$\sigma2$ and (B) $\sigma2$—$\sigma6$: comparison between prediction (solid black line for yielding; dashed black line for failure) and numerical simulations (red markers) [Colour figure can be viewed at wileyonlinelibrary.com]

5 | DISCUSSION OF THE RESULTS

5.1 | Yielding surface and failure locus numerical validation

The yielding and failure loci were validated by comparing the predicted values with the results of other three numerical simulations not used for the fitting; Figure 12 shows the results. The first simulation was carried out imposing two normal stresses with same magnitude but different sign ($\sigma_1 = -\sigma_2$; Figure 12A). The prediction in terms of yielding is accurate while the failure is slightly overestimated (around 15%). In the second analysis, a constant positive value of σ_2 (10 MPa) and an increasing shear stress σ_6 were applied (Figure 12B). To avoid over-constraining issues in the model, the shear was imposed in strain control and the normal stress in stress control. Both yielding and failure prediction are accurate with less than 5% error. In the last verification analysis, $\sigma_2 < 0$ and σ_6 were applied (Figure 12B). The yielding prediction is very precise, while failure is underestimated by around 10%.

By considering the distance between the numerical points and the surfaces and their relative positions, it is possible to quantify the error. If the failure or yielding condition is overestimated, the error is negative: This means that the numerical points are inside the surface. Vice versa, if it is underestimated, the error is positive. The mean value of the error and its standard deviation are 0.046 and 0.325 MPa, respectively, for the yielding condition, and −0.34 and 5.13 MPa respectively, for failure. As, for both cases, the mean value is close to zero with an allowable standard deviation (lower than 10% of the compressive strength), we can state that the prediction is accurate and sufficiently precise.

5.2 | Effect of as-manufactured geometry on multiaxial strength

The comparison between numerical prediction and experimental results in tension and compression reported in Figures 8 and 9 shows that as-manufactured geometry model prediction is accurate, while the prediction provided by as-designed geometry is significantly different. We observed two main contributions leading to different mechanical response and properties: the different relative density (as-manufactured cell is oversized) and the presence of localized imperfections, such as irregular strut borders and local geometrical defects. In this section, we

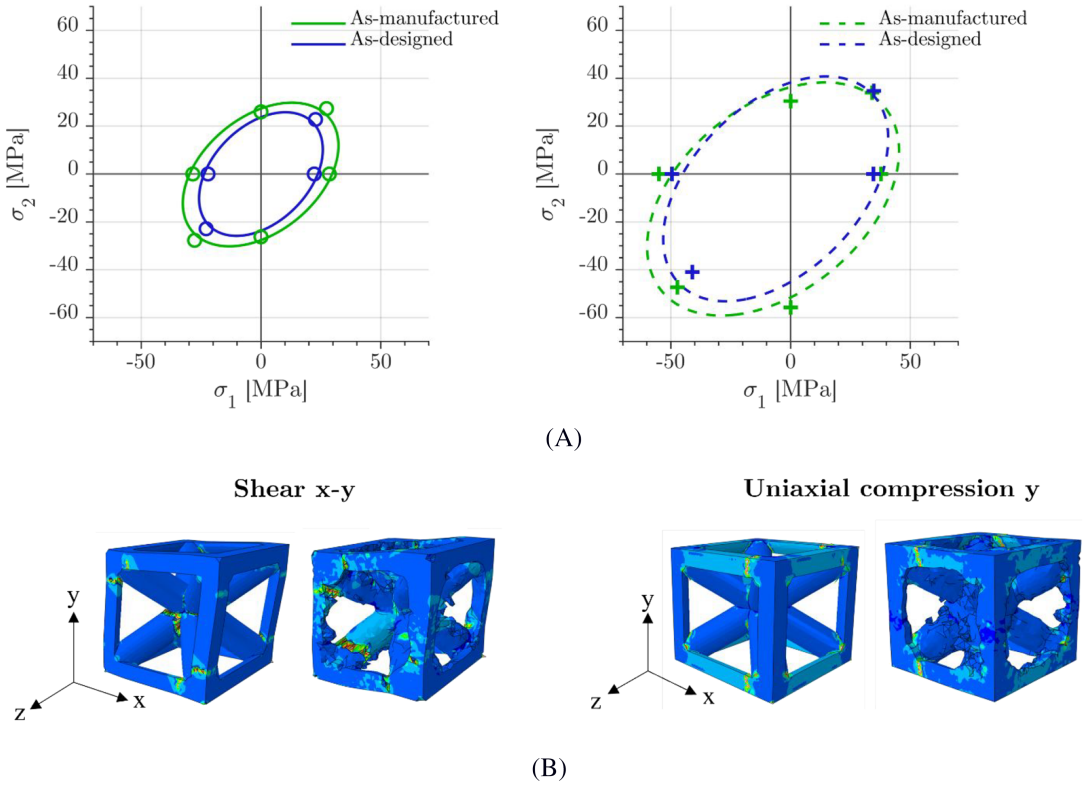

FIGURE 13 Comparison of multiaxial strength between as-designed and as-manufactured cell geometry: (A) yielding surface and failure locus for plane stress conditions ($\sigma 3 = 0$); (B) comparison of failure localizations predicted by the numerical models for shear and uniaxial compression conditions [Colour figure can be viewed at wileyonlinelibrary.com]

discuss the deviations introduced by the as-manufactured geometry on the multiaxial strength, by comparing failure and yielding loci found above with the ones obtained for the as-designed geometry. We repeated the procedure followed for as-manufactured geometry, simulating different multiaxial loading conditions, and then fitting the coefficients of yielding surface and failure locus. As as-designed cell shows a cubic symmetry, the expression in Equation 2 can be reduced to

$$F_n(\sigma_1+\sigma_2+\sigma_3)+F_{nn}\left(\sigma_1^2+\sigma_2^2+\sigma_3^2\right)+\overline{F_{nn}}\left(\sigma_4^2+\sigma_5^2+\sigma_6^2\right)+2F_c(\sigma_1\sigma_2+\sigma_1\sigma_3+\sigma_2\sigma_3)=1. \quad (3)$$

In this case, only four constants are to be fitted, the linear coefficient F_n, the quadratic coefficients F_{nn} and $\overline{F_{nn}}$, and the coupling coefficient F_c, leading to a considerably lower number of simulations to obtain a reliable fitting. Consequently, only seven simulations are needed: uniaxial, biaxial, and triaxial tension and compression (six simulations) and shear condition.

Figure 13 shows a comparison between the results for as-designed and as-manufactured cell models. In Figure 13A the yielding surfaces (left) and failure locus (right) for plane stress conditions ($\sigma_3 = 0$) are compared. The yielding surface of as-designed cell is an ellipse centered in the origin, and the axis coincides with the bisectors of I–III and II–IV quarters. The lower relative density makes the yielding locus of as-designed cell smaller than the one of as-manufactured cell, with a difference in uniaxial yielding limit of 15%. This difference is far less significant on the failure locus: the two ellipses are almost overlapped, especially if at least one of the two stress is positive (I, II, and IV quarters). For as-designed cell, the ratio between ultimate tensile strength and yielding stress is approximately 1.8, while for as-manufactured cell, it is 1.5, showing a more brittle behavior. The ultimate compressive strength, instead, is about two times bigger than yielding stress, for both geometries. As observed for numerical simulations, geometrical imperfections act as fracture trigger in struts subjected to tension with a detrimental effect on ultimate strength, while this effect is mitigated by compression.

Table 3 provides a comparison of yielding and failure limit stresses for as-manufactured and as-designed cell for the multiaxial loading conditions considered. As-manufactured cell ultimate strength is more sensitive to stress triaxiality: The ultimate strength of as-manufactured cell is 38.5 MPa for positive hydrostatic stress and −79.0 MPa for negative one, while the limits for as-designed cell are 47.3 and −112.7 MPa,

TABLE 3 Yielding limit and ultimate strength for the multiaxial loading conditions used for fitting the yielding and failure loci for as-manufactured and as-designed cells

		As-manufactured cell		As-designed cell	
Loading condition	**Dir.**	**Yielding limit (MPa)**	**Ultimate strength (MPa)**	**Yielding limit (MPa)**	**Ultimate strength (MPa)**
Uniaxial compression	*X*	−28.5	−55.0	−22.1	−49.5
	Y	−26.2	−55.7		
	Z	−27.0	−58.7		
Uniaxial tension	*X*	28.5	37.8	22.1	34.6
	Y	25.9	30.4		
	Z	27.0	38.0		
Biaxial compression	*X-Y*	−27.7	−47.3	−22.8	−41.0
	X-Z	−27.3	−41.8		
	Y-Z	−26.3	−46.7		
Biaxial tension	*X-Y*	27.3	34.0	22.8	34.7
	X-Z	26.9	39.5		
	Y-Z	25.9	32.5		
Negative hydrostatic stress	-	−31.4	−79.1	−29.5	−112.7
Positive hydrostatic stress	-	30.6	38.5	29.5	47.3
Shear	*X-Y*	22.5	31.7	17.9	28.1
	X-Z	22.2	32.3		
	Y-Z	21.7	30.6		

respectively. For shear conditions, the ultimate strength of as-designed cell (28.2 MPa) is comparable to the one of as-manufactured cell (30.7 MPa in *X*-*Y* directions), showing that the presence of geometrical imperfections combined with bending of vertical struts compensates the possible effects of cell oversizing in increasing the limit.

Both as-designed and as-manufactured cell models predict identical local failure mechanism (Figure 13B). For example, for shear condition (left), failure is localized in the diagonal strut subjects to tension and on vertical struts subjected to bending, while for uniaxial compression (right), failure is localized in horizontal struts subjected to tension. However, even if failure is localized in the same struts, the position of failure localization in the struts is different: for as-designed geometry is always localized at struts intersections, that introduce a singularity, while for as-manufactured geometry failure is localized in correspondence of a geometrical imperfection.

6 | CONCLUSIONS

In this work, the multiaxial yielding and numerical strength of an aluminum body centered cubic (SC-BCC) cell were studied numerically. Parent material was experimentally characterized in tension, and the GTN damage model was calibrated to predict material failure in numerical analyses. Tension and compression monotonic tests were performed on lattice samples. Experimental results were compared with numerical prediction to validate the accuracy of the damage model in predicting failure of lattices. By combining the use of the damage model with periodic boundary conditions for a single cell model, yielding and failure conditions for the homogenized metamaterial were studied. Based on the numerical results, it was found that the Tsai-Wu formulation describes yielding and failure condition well. Failure and yielding loci were validated numerically, and the effect on multiaxial strength of as-manufactured geometry obtained by the printing process was quantified.

The remarkable results obtained can be summarized as follows:

- Experimentally, it was found that failure of this type of structure with a relative density between 35% and 40% is driven by localized fracture. Neither elastic instability nor plastic collapse was observed in compression.
- The GTN model is able to predict failure of lattice samples. Good correlation with experiments in tension and compression was found. Characteristic curves, failure localizations, and failure mechanism are correctly described.
- A closed form based on the Tsai-Wu criterion for anisotropic material is proposed to describe the yielding surface and the failure locus of the SC-BCC lattice structure. The coefficients of the analytical expression were fitting using the results of multiaxial numerical simulations performed on single cell geometry, combining PBC, and damage model. The formulation was validated comparing the prediction and numerical results for multiaxial loading conditions not used for the fitting, showing good accuracy. We highlight that the results here shown are valid for this type of cell topology and geometric parameters, but the proposed method to assess multiaxial strength of lattices can be extended to other topologies that show a failure characterized by localized brittle fracture.
- We observed two main differences between as-designed and as-manufactured geometries. First, as-manufactured cell is oversized, with a higher relative density than as-designed cell. This aspect leads to a higher yielding limit and a more expanded yielding surface. Second, the manufacturing process introduced random imperfections and irregularities in struts bordered that act as fracture trigger.

ACKNOWLEDGMENTS

This research was done within the METAMatLab, a laboratory supported by Politecnico di Milano. The Italian Ministry of Education, University and Research is acknowledged for the support provided through the "Department of Excellence LIS4.0 - Lightweight and Smart Structures for Industry 4.0" project. The AlSi10Mg specimens were printed by BEAMIT, Fornovo di Taro (PR) Italy, while the CT scans were performed at Smart NDT, Villasanta (MB), Italy. Their support of research activities is greatly acknowledged. Open Access Funding provided by Politecnico di Milano within the CRUI-CARE Agreement.

DATA AVAILABILITY STATEMENT

Research data are not shared.

ORCID

Matteo Gavazzoni https://orcid.org/0000-0002-8481-7004
Stefano Beretta https://orcid.org/0000-0002-0824-8348
Stefano Foletti https://orcid.org/0000-0003-4140-2092

REFERENCES

1. Gibson LJ, Ashby MF. *Cellular Solids*. Cambridge University Press, 1997. https://doi.org/10.1017/CBO9781139878326
2. Ashby MF. The properties of foams and lattices. *Philos Trans R Soc a Math Phys Eng Sci*. 2006;364(1838):15-30. https://doi.org/10.1098/rsta.2005.1678

3. Ahmadi SM, Yavari SA, Wauthle R, et al. Additively manufactured open-cell porous biomaterials made from six different space-filling unit cells: The mechanical and morphological properties. *Materials (Basel)*. 2015;8(4):1871-1896. https://doi.org/10.3390/ma8041871
4. Amin Yavari S, Ahmadi SM, van der Stok J, et al. Effects of bio-functionalizing surface treatments on the mechanical behavior of open porous titanium biomaterials. *J Mech Behav Biomed Mater*. 2014;36:109-119. https://doi.org/10.1016/j.jmbbm.2014.04.010
5. Amin Yavari S, Ahmadi SM, Wauthle R, et al. Relationship between unit cell type and porosity and the fatigue behavior of selective laser melted meta-biomaterials. *J Mech Behav Biomed Mater*. 2015;43:91-100. https://doi.org/10.1016/j.jmbbm.2014.12.015
6. Hedayati R, Ahmadi SM, Lietaert K, et al. Isolated and modulated effects of topology and material type on the mechanical properties of additively manufactured porous biomaterials. *J Mech Behav Biomed Mater*. 2018;79(December 2017):254-263. https://doi.org/10.1016/j.jmbbm.2017.12.029
7. Arabnejad S, Burnett Johnston R, Pura JA, Singh B, Tanzer M, Pasini D. High-strength porous biomaterials for bone replacement: A strategy to assess the interplay between cell morphology, mechanical properties, bone ingrowth and manufacturing constraints. *Acta Biomater*. 2016;30:345-356. https://doi.org/10.1016/j.actbio.2015.10.048
8. Melancon D, Bagheri ZS, Johnston RB, Liu L, Tanzer M, Pasini D. Mechanical characterization of structurally porous biomaterials built via additive manufacturing: experiments, predictive models, and design maps for load-bearing bone replacement implants. *Acta Biomater*. 2017;63:350-368. https://doi.org/10.1016/j.actbio.2017.09.013
9. Bobbert FSL, Lietaert K, Eftekhari AA, et al. Additively manufactured metallic porous biomaterials based on minimal surfaces: a unique combination of topological, mechanical, and mass transport properties. *Acta Biomater*. 2017;53:572-584. https://doi.org/10.1016/j.actbio.2017.02.024
10. Lee S, Barthelat F, Moldovan N, Espinosa HD, Wadley HNG. Deformation rate effects on failure modes of open-cell Al foams and textile cellular materials. *Int J Solids Struct*. 2006;43(1):53-73. https://doi.org/10.1016/j.ijsolstr.2005.06.101
11. McKown S, Shen Y, Brookes WK, et al. The quasi-static and blast loading response of lattice structures. *Int J Impact Eng*. 2008;35(8):795-810. https://doi.org/10.1016/j.ijimpeng.2007.10.005
12. Maloney KJ, Fink KD, Schaedler TA, Kolodziejska JA, Jacobsen AJ, Roper CS. Multifunctional heat exchangers derived from three-dimensional micro-lattice structures. *Int J Heat Mass Transf*. 2012;55(9-10):2486-2493. https://doi.org/10.1016/j.ijheatmasstransfer.2012.01.011
13. Femmer T, Kuehne AJC, Wessling M. Estimation of the structure dependent performance of 3-D rapid prototyped membranes. *Chem Eng J*. 2015;273:438-445. https://doi.org/10.1016/j.cej.2015.03.029
14. Fink KD, Kolodziejska JA, Jacobsen AJ, Roper CS. Pyrolysis of heavy oil in the presence of supercritical water: the reaction kinetics in different phases. *AICHE J*. 2015;61(3):857-866. https://doi.org/10.1002/aic
15. Gibson LJ, Ashby MF. Mechanics of three-dimensional cellular materials. *Proc R Soc London, Ser a Math Phys Sci*. 1982;382(1782):43-59. https://doi.org/10.1098/rspa.1982.0088
16. Zhu HX, Knott JF, Mills NJ. Analysis of the elastic properties of open-cell foams with tetrakaidecahedral cells. *J Mech Phys Solids*. 1997;45(3):319-343.
17. Wallach JC, Gibson LJ. Mechanical behavior of a three-dimensional truss material. *Int J Solids Struct*. 2001;38(40-41):7181-7196. https://doi.org/10.1016/S0020-7683(00)00400-5
18. Ushijima K, Cantwell WJ, Mines RAW, Tsopanos S, Smith M. An investigation into the compressive properties of stainless steel micro-lattice structures. *J Sandw Struct Mater*. 2011;13(3):303-329. https://doi.org/10.1177/1099636210380997
19. Hassani B, Hinton E. A review of homogenization and topology optimization I - Homogenization theory for media with periodic structure. *Comput Structure*. 1998;69(6):707-717. https://doi.org/10.1016/S0045-7949(98)00131-X
20. Hassani B, Hinton E. A review of homogenization and topology opimization II—analytical and numerical solution of homogenization equations. *Comput Structure*. 1998;69(6):719-738. https://doi.org/10.1016/S0045-7949(98)00132-1
21. Arabnejad S, Pasini D. Mechanical properties of lattice materials via asymptotic homogenization and comparison with alternative homogenization methods. *Int J Mech Sci*. 2013;77:249-262. https://doi.org/10.1016/j.ijmecsci.2013.10.003
22. Deshpande VS, Fleck NA, Ashby MF. Effective properties of the octet-truss lattice material. *J Mech Phys Solids*. 2001;49(8):1747-1769.
23. Lee DW, Khan KA, Abu Al-Rub RK. Stiffness and yield strength of architectured foams based on the Schwarz Primitive triply periodic minimal surface. *Int J Plast*. 2017;95:1-20. https://doi.org/10.1016/j.ijplas.2017.03.005
24. Lampeas G, Diamantakos I, Ptochos E. Multifield modelling and failure prediction of cellular cores produced by selective laser melting. *Fatigue Fract Eng Mater Struct*. 2019;42(7):1534-1547. https://doi.org/10.1111/ffe.13008
25. Amani Y, Dancette S, Delroisse P, Simar A, Maire E. Compression behavior of lattice structures produced by selective laser melting: X-ray tomography based experimental and finite element approaches. *Acta Mater*. 2018;159:395-407. https://doi.org/10.1016/j.actamat.2018.08.030
26. Amani Y, Dancette S, Maire E, Adrien J, Lachambre J. Two-scale tomography based finite elementmodeling of plasticity and damage in aluminum foams. *Materials (Basel)*. 2018;11(10). 1-17. https://doi.org/10.3390/ma11101984
27. Drücker S, Schulze M, Ipsen H, Bandegani L, Hoch H, Kluge M, Fiedler B, "Experimental and numerical mechanical characterization of additively manufactured Ti6Al4V lattice structures considering progressive damage," *Int J Mech Sci* 2020;189:105986. https://doi.org/10.1016/j.ijmecsci.2020.105986
28. Pasini D, Guest JK. Imperfect architected materials: mechanics and topology optimization. *MRS Bull*. 2019;44(10):766-772. https://doi.org/10.1557/mrs.2019.231
29. Benedetti M, du Plessis A, Ritchie RO, Dallago M, Razavi SMJ, Berto F. Architected cellular materials: a review on their mechanical properties towards fatigue-tolerant design and fabrication. *Mater Sci Eng R Reports*. 2021;144:100606. https://doi.org/10.1016/j.mser.2021.100606

30. Simone AE, Gibson LJ. Effects of solid distribution on the stiffness. *Acta Mater*. 1998;46(6):2139-2150.
31. Chen C, Lu TJ, Fleck NA. Effect of imperfections on the yielding of two-dimensional foams. *J Mech Phys Solids*. 1999;47(11):2235-2272. https://doi.org/10.1016/S0022-5096(99)00030-7
32. Symons DD, Fleck NA. The imperfection sensitivity of isotropic two-dimensional elastic lattices. *J Appl Mech Trans ASME*. 2008;75(5):051011. https://doi.org/10.1115/1.2913044
33. Campoli G, Borleffs MS, Amin Yavari S, Wauthle R, Weinans H, Zadpoor AA. Mechanical properties of open-cell metallic biomaterials manufactured using additive manufacturing. *Maternite*. 2013;49:957-965. https://doi.org/10.1016/j.matdes.2013.01.071
34. Liu L, Kamm P, García-Moreno F, Banhart J, Pasini D. Elastic and failure response of imperfect three-dimensional metallic lattices: the role of geometric defects induced by Selective Laser Melting. *J Mech Phys Solids*. 2017;107:160-184. https://doi.org/10.1016/j.jmps.2017.07.003
35. Raghavendra S, Molinari A, Dallago M, et al. Uniaxial static mechanical properties of regular, irregular and random additively manufactured cellular materials: nominal vs. real geometry. *Forces Mech*. 2021;2(November 2020):100007. https://doi.org/10.1016/j.finmec.2020.100007
36. Tancogne-Dejean T, Mohr D. Elastically-isotropic truss lattice materials of reduced plastic anisotropy. *Int J Solids Struct*. 2018;138:24-39. https://doi.org/10.1016/j.ijsolstr.2017.12.025
37. Gavazzoni M, Boniotti L, Foletti S. Influence of specimen size on the mechanical properties of microlattices obtained by selective laser melting. *Proc Inst Mech Eng Part C J Mech Eng Sci*. 2019;235(10):1774-1787. https://doi.org/10.1177/0954406219869741
38. Tsai SW, Wu EM. A general theory of strength for anisotropic materials. *J Compos Mater*. 1971;5(1):58-80. https://doi.org/10.1177/002199837100500106
39. Murchio S, Dallago M, Zanini F, et al. Additively manufactured Ti–6Al–4V thin struts via laser powder bed fusion: Effect of building orientation on geometrical accuracy and mechanical properties. *J Mech Behav Biomed Mater*. 2021;119:104495. https://doi.org/10.1016/j.jmbbm.2021.104495
40. Boniotti L, Beretta S, Patriarca L, Rigoni L, Foletti S. Experimental and numerical investigation on compressive fatigue strength of lattice structures of AlSi7Mg manufactured by SLM. *Int J Fatigue*. 2019;128:105181. https://doi.org/10.1016/j.ijfatigue.2019.06.041
41. Boniotti L, Foletti S, Beretta S, Patriarca L. Analysis of strain and stress concentrations in micro-lattice structures manufactured by SLM. *Rapid Prototyp J*. 2020;26(2):370-380. https://doi.org/10.1108/RPJ-10-2018-0270
42. Köhnen P, Haase C, Bültmann J, Ziegler S, Schleifenbaum JH, Bleck W. Mechanical properties and deformation behavior of additively manufactured lattice structures of stainless steel. *Mater des*. 2018;145:205-217. https://doi.org/10.1016/j.matdes.2018.02.062
43. Drücker S, Inman S, and Fiedler B, "Simulation and optimization of the load introduction geometry of additively manufactured lattice structure specimens" 2018;(June):24-28.
44. Simulia, "Abaqus."
45. Gurson AL. Continuum theory of ductile rupture by void nucleation and growth: part I—yield criteria and flow rules for porous ductile media. *J Eng Mater Technol*. 1977;99(1):2-15. https://doi.org/10.1115/1.3443401
46. Tvergaard V. Influence of voids on shear band instabilities under plane strain conditions. *Int J Fract*. 1981;17(4):389-407. https://doi.org/10.1007/BF00036191
47. Tvergaard V, Needleman A. Analysis of the cup-cone round tensile fracture. *Acta Metall*. 1984;32(1):157-169. https://doi.org/10.1016/0001-6160(84)90213-X
48. Needleman A, Tvergaard V. An analysis of ductile rupture in notched bars. *J Mech Phys Solids*. 1984;32(6):461-490. https://doi.org/10.1016/0022-5096(84)90031-0
49. Farahani BV, Belinha J, Tavares PJ, Moreira PMGP. Elastoplastic response and failure assessment of steel alloys: Empirical and computational analyses. *Fatigue Fract Eng Mater Struct*. 2019;42(6):1247-1261. https://doi.org/10.1111/ffe.12914
50. Tvergaard V. On localization in ductile materials containing spherical voids. *Int J Fract*. 1982;18(4):237-252. https://doi.org/10.1007/BF00015686
51. Terada K, Hori M, Kyoya T, Kikuchi N. Simulation of the multi-scale convergence in computational homogenization approaches. *Int J Solids Struct*. 2000;37(16):2285-2311. https://doi.org/10.1016/S0020-7683(98)00341-2
52. Tyrus JM, Gosz M, DeSantiago E. A local finite element implementation for imposing periodic boundary conditions on composite micromechanical models. *Int J Solids Struct*. 2007;44(9):2972-2989. https://doi.org/10.1016/j.ijsolstr.2006.08.040
53. Schmitz A, Horst P. A finite element unit-cell method for homogenised mechanical properties of heterogeneous plates. *Compos Part a Appl Sci Manuf*. 2014;61:23-32. https://doi.org/10.1016/j.compositesa.2014.01.014
54. Banabic D, Kuwabara T, Balan T, Comsa DS, Julean D. Non-quadratic yield criterion for orthotropic sheet metals under plane-stress conditions. *Int J Mech Sci*. 2003;45(5):797-811. https://doi.org/10.1016/S0020-7403(03)00139-5

How to cite this article: Gavazzoni M, Pisati M, Beretta S, Foletti S. Multiaxial static strength of a 3D printed metallic lattice structure exhibiting brittle behavior. *Fatigue Fract Eng Mater Struct*. 2021;44(12):3499-3516. doi:10.1111/ffe.13587